Graph Convolutional Networks for Simulating Multi-phase Flow and Transport in Porous Media

Jiamin Jiang

Chevron Technical Center

Bo Guo

Hydrology and Atmospheric Sciences, The University of Arizona

Abstract

Numerical simulation of multi-phase fluid dynamics in porous media is critical for many subsurface applications. Data-driven surrogate modeling provides computationally inexpensive alternatives to high-fidelity numerical simulators. While the commonly used convolutional neural networks (CNNs) are powerful in approximating partial differential equation solutions, it remains challenging for CNNs to handle irregular and unstructured simulation meshes. However, subsurface simulation models often involve unstructured meshes with complex mesh geometries, which limits the application of CNNs. To address this challenge, here we construct surrogate models based on Graph Convolutional Networks (GCNs) to approximate the spatial-temporal solutions of multi-phase flow and transport processes. We propose a new GCN architecture suited to the hyperbolic character of the coupled PDE system, to better capture the saturation dynamics. Results of 2D heterogeneous test cases show that our surrogates predict the evolutions of the pressure and saturation states with high accuracy, and the predicted rollouts remain stable for multiple timesteps. Moreover, the GCN-based models generalize well to irregular domain geometries and unstructured meshes that are unseen in the training dataset.

1. Introduction

Dynamics of multiple fluid phases in porous media are critical for many applications in Earth's subsurface, including oil and gas recovery, groundwater remediation, geological CO₂ sequestration, and subsurface hydrogen storage. Numerical simulations play an increasingly important role in understanding, quantifying, and controlling these multiphase flow processes. Predicting the evolution of subsurface fluid dynamics requires solving partial differential equations (PDEs) governing the multi-phase flow and transport processes. These PDEs are often highly nonlinear and exhibit an intricate mixture of elliptic and hyperbolic characteristics, posing challenges to numerical methods. Moreover, significant uncertainties are present in the model parameters due to data scarcity in the subsurface. As a result, many model simulation runs (e.g., thousands) are required to quantify the uncertainties propagated from the parameters to the predictions. Therefore, computationally efficient simulation techniques are critical for subsurface applications.

The deep learning revolution (LeCun et al. 2015; Krizhevsky et al. 2017) has dramatically changed scientific fields such as computer vision and natural language processing. More recently, deep learning algorithms have been extended towards constructing datadriven surrogate models to approximate the solutions of PDEs, particularly in the context

Email address: jiamin.jiang@chevron.com (Jiamin Jiang)

^{*}Corresponding author

of fluid dynamics (Guo et al. 2016; Kutz 2017; Long et al. 2018; Bar-Sinai et al. 2019; Santos et al. 2020; Li et al. 2020; Lu et al. 2021; Vinuesa and Brunton 2022). Compared to high-fidelity numerical simulators, a learned simulator can provide much faster predictions, especially for high-dimensional nonlinear systems.

A number of studies have applied image-based approaches and snapshots of simulation data over a spatially discretized input domain for surrogate modeling of subsurface flow and transport problems. Most of these works leverage convolutional neural networks (CNNs) to learn the nonlinear mappings from the input properties (e.g., permeability) to the output states (pressure and saturation) on regular Cartesian meshes (Mo et al. 2019; Tang et al. 2020; Wang and Lin 2020; Wen et al. 2021; Zhang et al. 2021; Jiang et al. 2021; Yan et al. 2022; Maldonado-Cruz and Pyrcz 2022). While CNNs are powerful in approximating PDE solutions, they are restricted to a specific discretization of the physical domain in which they are trained. Due to the inherent limitations of standard convolution operations, it remains challenging for CNNs to handle irregular and unstructured simulation meshes. However, driven by the need to accurately characterize complex geological features and heterogeneity, subsurface simulation models often involve corner-point and unstructured meshes with skewed and degenerate mesh geometries. These complexities limit the application of CNN-based models for subsurface problems. Note that Maucec and Jalali (2022) recently applied the interaction networks (Battaglia et al. 2016) for surrogate modeling of a two-phase incompressible flow problem, but their surrogate leads to large prediction errors of the pressure field.

Graph Neural Networks (GNNs) have successfully been employed to learn the dynamic evolutions of PDEs, under mesh-based simulation frameworks (Pfaff et al. 2020; Belbute-Peres et al. 2020; Iakovlev et al. 2020; Chen et al. 2021; Brandstetter et al. 2022; Pilva and Zareei 2022). In contrast to CNNs, GNNs naturally enable operating on unstructured meshes with complex domain boundaries. A simulation mesh can be viewed as a graph composed of nodes, and a set of edges representing the connectivity between the nodes. The key idea of GNNs is to aggregate and propagate the local information of system states from their neighborhoods into node representations, through multiple message passing layers (Kipf and Welling 2016; Gilmer et al. 2017).

In the present work, we apply Graph Convolutional Networks (GCNs) to learn surrogate models for predicting the spatial-temporal solutions of multi-phase flow and transport in porous media. We seperately design two GCN architectures that are suited to the elliptic and hyperbolic characteristics of the coupled PDE system, to better capture the pressure and saturation dynamics. The GCN-based models are trained by supervising on the per-node output states. We evaluate the prediction performance of the trained surrogates using 2D heterogeneous cases. The results show that our surrogates predict the dynamic evolutions with high accuracy, and the predicted rollouts remain stable for multiple timesteps. Moreover, our GCN models generalize well to irregular domain geometries and unstructured meshes that are not present in the training dataset.

2. Mathematical model and discretization

2.1. Immiscible multi-phase flow in porous media

We consider compressible and immiscible flow and transport in porous media with n_p number of phases. The mass-conservation equation for phase l ($l \in \{1,...,n_p\}$) can be written as

$$\frac{\partial}{\partial t} (\phi \rho_l s_l) + \nabla \cdot (\rho_l v_l) - \rho_l q_l = 0, \tag{1}$$

where t is time. ϕ is rock porosity. q_l is the volumetric injection or pumping rate of wells (source or sink term). ρ_l is phase density. s_l is phase saturation, which is constrained by

$$\sum_{l} s_l = 1,\tag{2}$$

The Darcy phase velocity, v_l , is expressed as

$$\mathbf{v}_l = -k\lambda_l \left(\nabla p_l - \rho_l g \nabla z \right). \tag{3}$$

where k is rock permeability. p_l is phase pressure. g is gravitational acceleration and z is depth (assuming positive downward). $\lambda_l = k_{rl}/\mu_l$ is phase mobility, where k_{rl} and μ_l are relative permeability and fluid viscosity, respectively.

For oil-water flow that only involves two fluid phases, Eq. (1) can be simplified to

$$\frac{\partial}{\partial t} (\phi \rho_o s_o) + \nabla \cdot (\rho_o v_o) - \rho_o q_o = 0, \tag{4}$$

$$\frac{\partial}{\partial t} \left(\phi \rho_w s_w \right) + \nabla \cdot (\rho_w \mathbf{v}_w) - \rho_w q_w = 0, \tag{5}$$

with the saturation constraint as $s_o + s_w - 1 = 0$.

2.2. Fully-implicit discretization

To solve the PDE system from Eq. (1), we apply a finite volume method that discretizes the simulation domain into a mesh consisting of n_b cells and the fully-implicit scheme for the time discretization

$$\frac{|\Omega_i|}{\Delta t} \left((\phi_i \rho_{l,i} s_{l,i})^{n+1} - (\phi_i \rho_{l,i} s_{l,i})^n \right) - \sum_{j \in adj(i)} (\rho_{l,ij} v_{l,ij})^{n+1} - Q_{l,i}^{n+1} = 0, \tag{6}$$

where $i \in \{1, ..., n_b\}$ is cell index, $|\Omega_i|$ is cell volume, (ij) corresponds to the interface between cells i and j. Superscripts represent timesteps, and Δt is timestep size.

The discrete phase flux based on the two-point flux approximation can be written as

$$v_{l,ij} = T_{ij}\lambda_{l,ij}\Delta\Phi_{l,ij},\tag{7}$$

where $\Delta\Phi_{l,ij} = \Delta p_{l,ij} - g_{l,ij}$ is the phase-potential difference with the discrete weights $g_{l,ij} = \rho_{l,ij} g \Delta z_{ij}$. The phase mobility $\lambda_{l,ij}$ is evaluated using the Phase-Potential Upwinding (PPU) scheme (Sammon 1988; Brenier and Jaffré 1991). In PPU, the mobility of each phase is treated separately according to the sign of the phase-potential difference. The upwinding criterion is given as

$$\lambda_{l,ij} = \begin{cases} \lambda_l(s_i), & \Delta \Phi_{l,ij} \ge 0\\ \lambda_l(s_j), & \text{otherwise} \end{cases}$$
 (8)

where $s_i = \{s_{l,i}\}_{l \in \{1,...,n_p\}}$ denotes the saturations of cell i.

The total face transmissibility T_{ij} combines two half-transmissibilities in a half of the harmonic average

$$T_{ij} = \frac{T_i T_j}{T_i + T_j}, \qquad T_i = \frac{k_i A_{ij}}{d_i}. \tag{9}$$

where A_{ij} denotes the interface area, k_i is the permeability of cell i, and d_i is the length from the cell centroid to the interface.

In the finite volume formulation, the discrete source (or sink) term for a mesh cell containing a well (referred to as well cell) is written as

$$Q_{l,i} = WI_i \left(\rho_l \lambda_l \right)_i \left(p_l - p^W \right)_i, \tag{10}$$

which represents the well flux for phase l in cell i. $p_{l,i}$ is well-cell pressure, p_i^W is well-bore pressure, and WI_i is well index.

The discretized nonlinear system, written in a residual format, has the following form

$$\mathcal{R}(\boldsymbol{u}^{n+1}) = 0 \tag{11}$$

where u represents the state variables (pressure and saturation) of mesh cells. The nonlinear system is often solved using the Newton method, which performs multiple iterations until convergence. For each timestep, with the solution u^n , and a chosen timestep size Δt , the new state u^{n+1} is obtained.

3. Surrogate models

A simulator \mathbb{H} maps the current state of mesh cells to the next timestep state. We denote a simulated rollout trajectory as $(\boldsymbol{u}^0, \boldsymbol{u}^1, ..., \boldsymbol{u}^{n_t})$, which is computed iteratively by $\boldsymbol{u}^{n+1} = \mathbb{H}(\boldsymbol{u}^n)$ for every timestep.

The goal of our surrogate learning task is to replace the computationally expensive high-fidelity simulator with surrogate simulators that predict the next state

$$\boldsymbol{u}^{n+1} \approx \widehat{\boldsymbol{u}}^{n+1} = \mathbb{N}\left(\boldsymbol{u}^n; \Theta\right), \tag{12}$$

where \mathbb{N} is a next-step prediction model based on GNN, whose parameters Θ can be optimized for some training objectives. $\widehat{\boldsymbol{u}}^{n+1}$ indicates the predicted state from the surrogate model. Given the initial state \boldsymbol{u}^0 , \mathbb{N} (; Θ) can rapidly produce a rollout trajectory of states $(\boldsymbol{u}^0, \widehat{\boldsymbol{u}}^1, ..., \widehat{\boldsymbol{u}}^{n_t})$, where n_t is the number of timesteps.

The coupled multi-phase system (1) has an intricate mixture of elliptic and hyperbolic

The coupled multi-phase system (1) has an intricate mixture of elliptic and hyperbolic characteristics. It is beneficial to employ specialized GNN architectures suitable for the specific characteristics of the coupled system. Therefore in the present work we seperately design and train two models that compute the solutions of pressure and saturation in a sequential manner as

$$\begin{cases}
\widehat{\boldsymbol{p}}^{n+1} = \mathbb{N}_p \left(\boldsymbol{p}^n, \boldsymbol{s}^n; \Theta_p \right), \\
\widehat{\boldsymbol{s}}^{n+1} = \mathbb{N}_s \left(\widehat{\boldsymbol{p}}^{n+1}, \boldsymbol{s}^n; \Theta_s \right).
\end{cases}$$
(13)

where \mathbb{N}_p and \mathbb{N}_s represent respectively the pressure and saturation models. At each time step, the saturation model takes the input from the pressure model.

The above process can be written using a compact operator as

$$\left[\widehat{\boldsymbol{p}}^{n+1}, \widehat{\boldsymbol{s}}^{n+1}\right] = \mathbb{N}_s \circ \mathbb{N}_p \left(\boldsymbol{p}^n, \boldsymbol{s}^n; \Theta_p, \Theta_s\right). \tag{14}$$

4. Graph Neural Networks

We leverage the power of GNNs to construct data-driven surrogate simulators to approximate the PDE solutions (Equation (14)). GNNs provide a flexible and efficient way to operate over data that are structured as graphs, naturally fitting mesh-based simulations (Pfaff et al. 2020; Pilva and Zareei 2022).

Let G = (X, E) be graph representation (**Fig. 1**) of a simulation mesh with nodes X (blue dots) where \mathbf{x}_i denotes the cell centroid, and undirected edges E (red line segments) where e_{ij} represents the connecting neighboring cells at \mathbf{x}_i and \mathbf{x}_j . $\mathcal{N}(i)$ is the set of adjacent nodes around node i. We further denote the node and edge features by \mathbf{u}_i and \mathbf{e}_{ij} respectively.

4.1. Message Passing Framework

A GNN-based model consists of a stack of neural network layers, each aiming to aggregate local neighborhood information, i.e., features of neighbors, around each node and then passes this aggregated information on to the next layer (Kipf and Welling 2016). The fundamental operation in GNNs is the message-passing procedure, which updates the feature vector of each node based on the features of its neighboring nodes. The message-passing rule is generally formulated as (Gilmer et al. 2017)

$$\mathbf{u}_{i}' = \gamma \left(\mathbf{u}_{i}, \bigoplus_{j \in \mathcal{N}(i)} \psi \left(\mathbf{u}_{i}, \mathbf{u}_{j}, \mathbf{e}_{ij} \right) \right),$$
 (15)

where \bigoplus denotes a differentiable, permutation-invariant function (e.g., summation, mean, or maximum), and γ and ψ are differentiable neural networks such as MultiLayer Perceptrons (MLPs). Each subsequent message-passing layer contains a separate set of network parameters, and operates on the output u_i' of the previous layer.

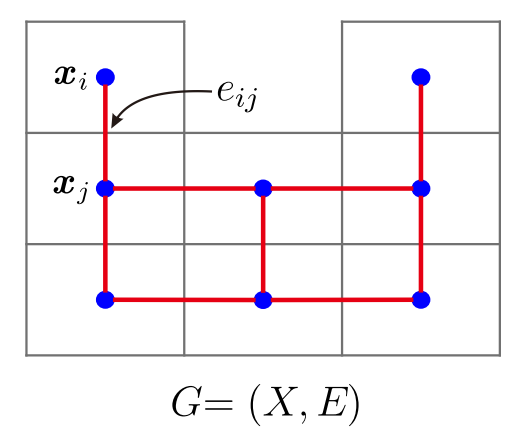


Figure 1: Schematic of the graph representation of a simulation mesh. Blue dots indicate nodes (cell centroids), and red segments indicate edges (cell connections).

In our work, we consider weighted graphs and employ the GCN operator, GraphConv, from Morris et al. (2019). At layer m, the new node features are updated as

$$\boldsymbol{u}_{i}^{(m+1)} = \sigma \left(\mathbf{W}_{1} \boldsymbol{u}_{i}^{(m)} + \mathbf{W}_{2} \sum_{j \in \mathcal{N}(i)} w_{ij} \cdot \boldsymbol{u}_{j}^{(m)} \right), \tag{16}$$

where \mathbf{W}_1 and \mathbf{W}_2 are parameter matrices, w_{ij} denotes the edge weight, and σ denotes a non-linear activation function, e.g., ReLU or Tanh.

We additionally utilize the edge convolution operator, EdgeConv, from Wang et al. (2019). EdgeConv exploits local geometric structures by constructing a local graph and applying convolution operations on the edges connecting neighboring pairs of nodes. The layer output can be computed by

$$\mathbf{u}_{i}^{(m+1)} = \max_{j \in \mathcal{N}(i)} \Psi\left(\mathbf{u}_{i}^{(m)}, \mathbf{u}_{j}^{(m)} - \mathbf{u}_{i}^{(m)}\right).$$
(17)

where Ψ denotes an MLP. As can be seen, the max aggregation operation is used on the edge features associated with all the edges emanating from a node.

5. Model architectures

In this section, we present the detailed surrogate models which can predict the next-step dynamic states of the coupled PDE system. Our GCN models have an Encoder-Processor-Decoder structure. Schematic of a general GCN model architecture is plotted in **Fig. 2**. The node features are first encoded into latent vectors of size n_H . The input features \boldsymbol{u}_i^n of mesh node i for each timestep contain the dynamic variables (pressure and saturation), permeability, and pore volume. A one-hot vector indicating node type (reservoir, production, and injection nodes), and well index are also added. We assign the transmissibility T_{ij} of each cell interface as edge weight. Each feature is scaled individually to [0,1] using the min-max normalization method. The Decoder extracts one output state $(\hat{\boldsymbol{p}}^{n+1} \text{ or } \hat{\boldsymbol{s}}^{n+1})$ from the latent node features after the final processing layer. The Encoder and Decoder are two-layer MLPs with ReLU nonlinearities except for the output layer of the Decoder, after which we do not apply any nonlinearity.

The Processor of the pressure model \mathbb{N}_p is constructed by stacking 7 identical Graph-Conv layers with the mean aggregation operation and ReLU nonlinearities, to obtain a sequence of updated latent features. For the \mathbb{N}_s model, we propose a combined architecture (3 EdgeConv followed by 5 GraphConv layers with max aggregation), which is

found to be quite effective for capturing the hyperbolic (saturation) solution. The Tanh activation function is applied. The sizes of hidden units for \mathbb{N}_p and \mathbb{N}_s are $n_{Hp}=32$ and $n_{Hs}=128$, respectively.

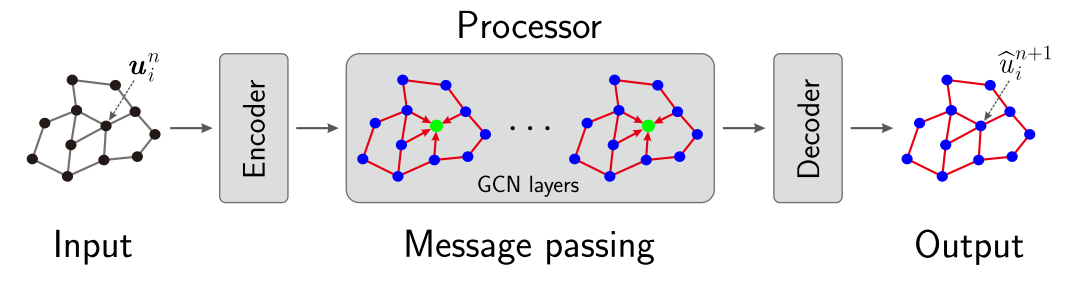


Figure 2: Schematic of a general GCN model architecture.

6. Training procedure

We train the GCN models using the dynamic state pairs $(\boldsymbol{u}^n; \boldsymbol{u}^{n+1})$ from n_Y number of simulated rollout trajectories. We employ a mean squared error loss between predictions $\hat{\boldsymbol{u}}_y^n$ and their corresponding ground truth values \boldsymbol{u}_y^n (simulator reference). The L_2 loss function is minimized through

$$\Theta^* = \underset{\Theta}{\operatorname{argmin}} \frac{1}{n_Y} \frac{1}{n_t} \sum_{y=1}^{n_Y} \sum_{n=1}^{n_t} \| \widehat{\boldsymbol{u}}_y^n - \boldsymbol{u}_y^n \|_2^2$$
 (18)

where n_t is the number of timesteps, and u_y^n denotes either pressure or saturation of every mesh node, at time t_n , for training sample y.

Modeling a complex time-dependent PDE system requires the model to mitigate error accumulation over long rollout trajectories (Sanchez-Gonzalez et al. 2020). Because we only train our surrogates on ground-truth one-step data, we corrupt the input saturation states with normal noise N_s (0, $\sigma_s = 0.02$). In this way, the rollouts of multiple timesteps from trained models become robust to their own noisy, previous predictions as input.

7. Surrogate model evaluations

We explore the prediction performance of the surrogate models and their generalization capabilities on out-of-training domain shapes and meshes. As an example, we consider 2D reservoir models in the x-y domain containing two wells (one injector and one producer) that operate under constant bottom-hole pressure (BHP). No-flow boundary condition is specified at the reservoir boundaries. The set-up of the base model is summarized in Table 1. Quadratic relative permeabilities are used. Capillary pressure is neglected. Total simulation time is 100 days, with a number of 20 timesteps.

There are 160 high-fidelity simulation runs as training data samples with random well locations and rock properties. The realizations of heterogeneous permeability and porosity fields are generated using a Gaussian distribution. The surrogate models are trained on a NVIDIA Tesla V100 GPU using the Adam optimizer (Kingma and Ba 2014) with learning rate 1e-4. The training loss (MSE) curves are plotted in **Fig. 3**.

It takes around 2 and 4 hours to train the pressure and saturation models, respectively. Note that the training times can be reduced by optimizing the hyperparameters of GCNs, and the learning rate schedule of the optimizer. Moreover, the large numbers of training epochs currently used are actually not necessary to reach reasonably low prediction errors. The trained models can predict a rollout trajectory in 0.1 seconds, achieving a significant reduction of computational time compared with the high-fidelity simulator, which requires about 22 seconds for a simulation run.

Table 1: Set-up of the base model

Parameter	Value	Unit
Model sizes (x, y, z)	182, 182, 3	m
Initial pressure	2000	psi
Initial water saturation	0.01	
Water viscosity	1.0	cР
Oil viscosity	2.0	cР
Rock compressibility	1e-8	1/bar
Oil compressibility	1e-4	1/bar
Production BHP	1800	psi
Injection BHP	2200	psi
Total simulation time	100	day
Timestep size	5	day

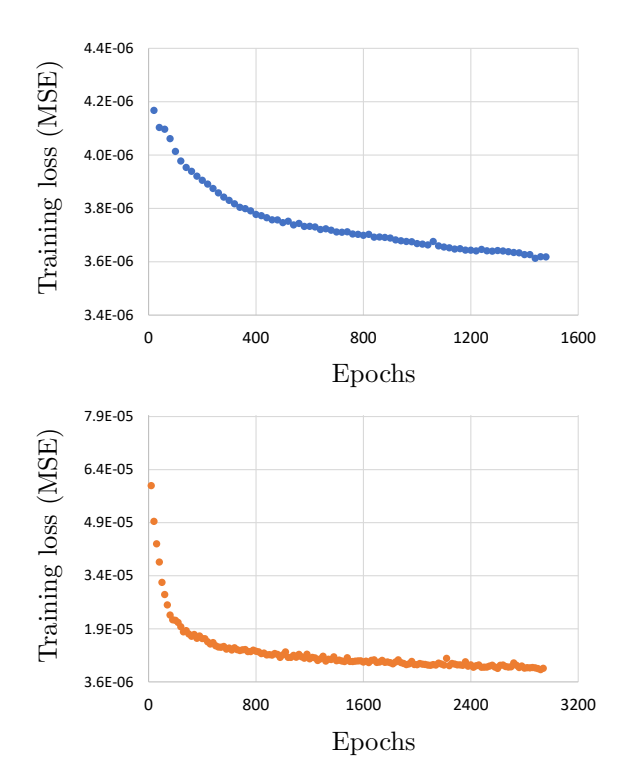


Figure 3: Training loss (MSE) curves of the pressure (upper) and saturation (lower) models.

7.1. Regular Cartesian mesh

We first present the predictions of three representative testing samples on a regular 60×60 Cartesian mesh. The rock property fields of the three cases are shown in **Fig. 4**, **Fig. 6** and **Fig. 8**, respectively.

We only compare the solution profiles (pressure and water saturation) at the end of the simulation between the surrogate (prediction) and high-fidelity (ground truth) simulators, because the solutions at the final time of a rollout trajectory should exhibit the largest accumulated errors. The pressure and water saturation profiles of the three cases are shown in Fig. 5, Fig. 7 and Fig. 9, respectively. As can be seen, the GCN-based surrogate models accurately capture the evolutions of the pressure and saturation states, with very low mean errors in all the three cases. It is important to note that even though our models were trained on the next-step predictions, the rollouts remain stable for multiple steps.

We can also see that the pressure model is capable of providing physically smooth pressure solutions. The saturation fields are strongly impacted by the well locations and heterogeneous rock properties. The saturation model based on our new GCN architecture incorporating EdgeConv (17) can reproduce both the shapes and heterogeneous details of the discontinuous saturation fronts quite well. Note that relatively large saturation differences are mainly observed near the water fronts.

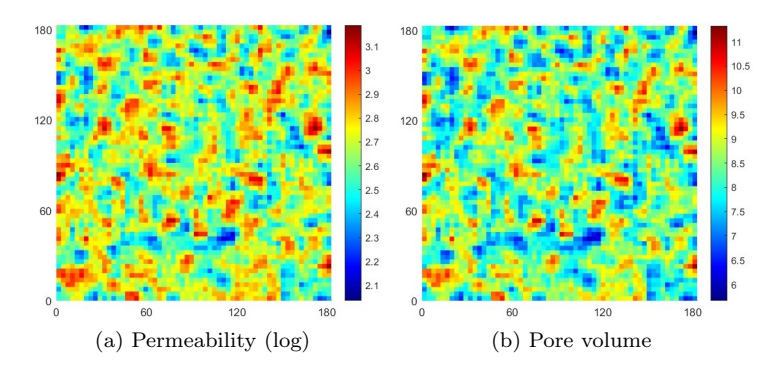


Figure 4: Permeability (md) and pore volume fields of Case 1 on the regular Cartesian mesh.

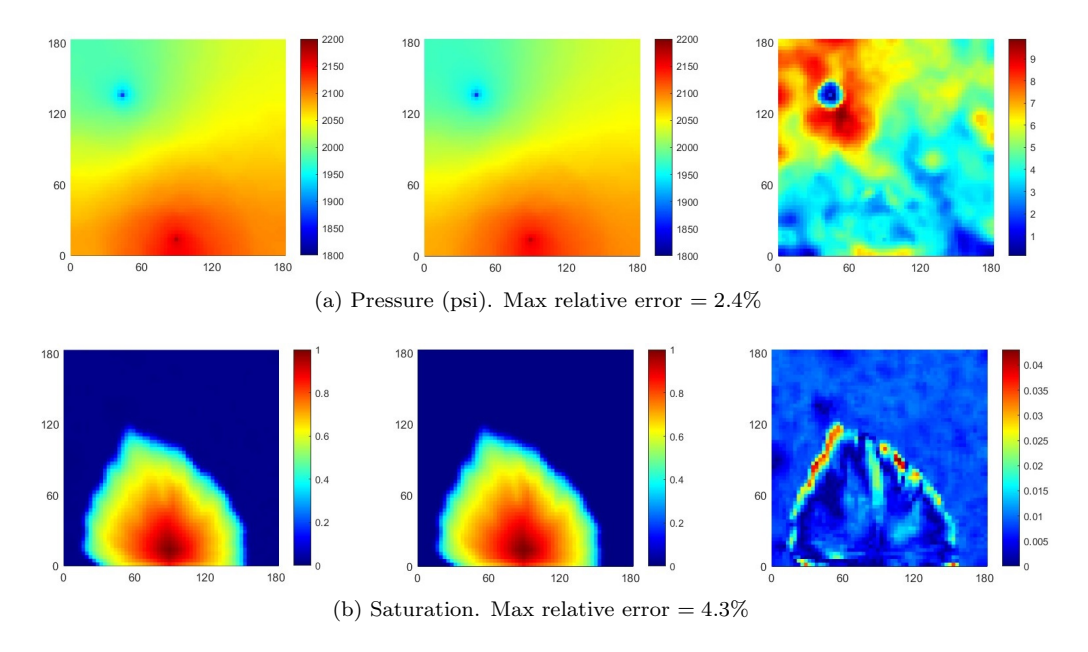


Figure 5: Prediction (left), ground truth (middle), and absolute difference (right) profiles of Case 1 on the regular Cartesian mesh.

To demonstrate the improvement due to EdgeConv, here we additionally show the results from a GCN model with only 7 GraphConv layers (without EdgeConv) and the max aggregation operation. The water saturation profiles of the three cases are shown in Fig. 10. Although the model (GraphConv) captures the overall shapes of the saturation fields with reasonable accuracy, greater errors are evident near the water fronts. Moreover, some heterogeneous details inside the water plume are smeared out, compared with the model with the combined architecture (EdgeConv+GraphConv). The mean relative errors of the invaded region (saturation bigger than the residual value) from the two saturation models are reported in Table 2.

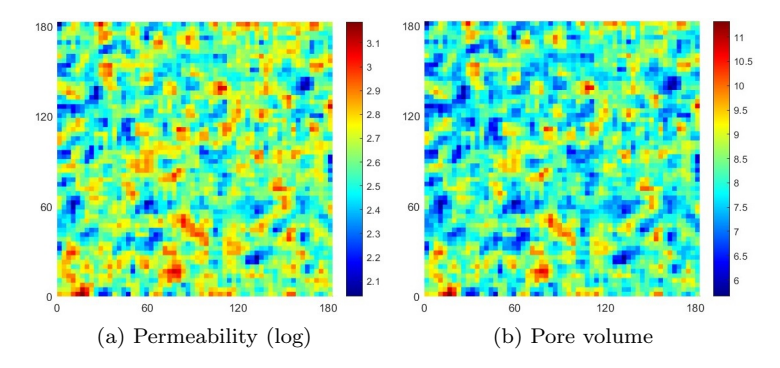


Figure 6: Permeability (md) and pore volume fields of Case 2 on the regular Cartesian mesh.

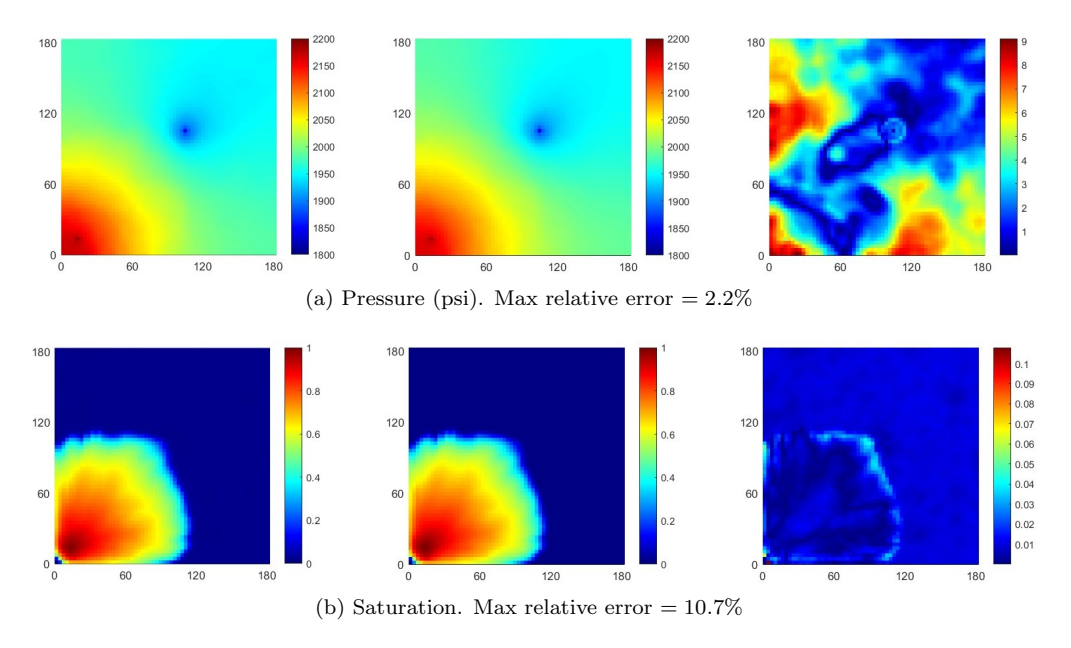


Figure 7: Prediction (left), ground truth (middle), and absolute difference (right) profiles of Case 2 on the regular Cartesian mesh.

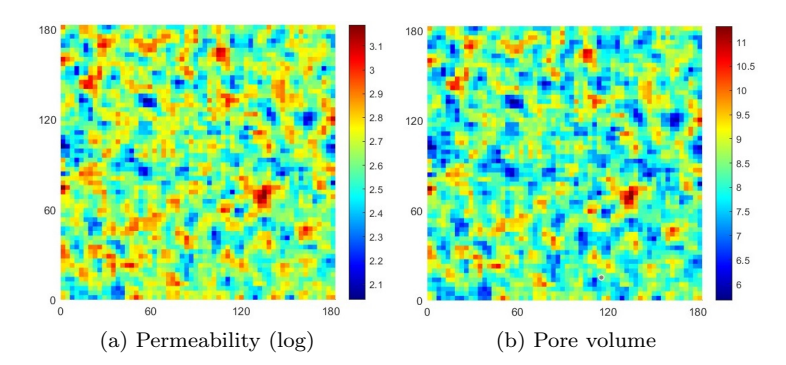


Figure 8: Permeability (md) and pore volume fields of Case 3 on the regular Cartesian mesh.

7.2. Irregular Cartesian mesh

We further evaluate the generalization ability of the trained surrogate simulators, using two test samples with irregular mesh geometries. The rock property fields of the two cases on irregular Cartesian mesh are shown in Fig. 11 and Fig. 13, respectively.

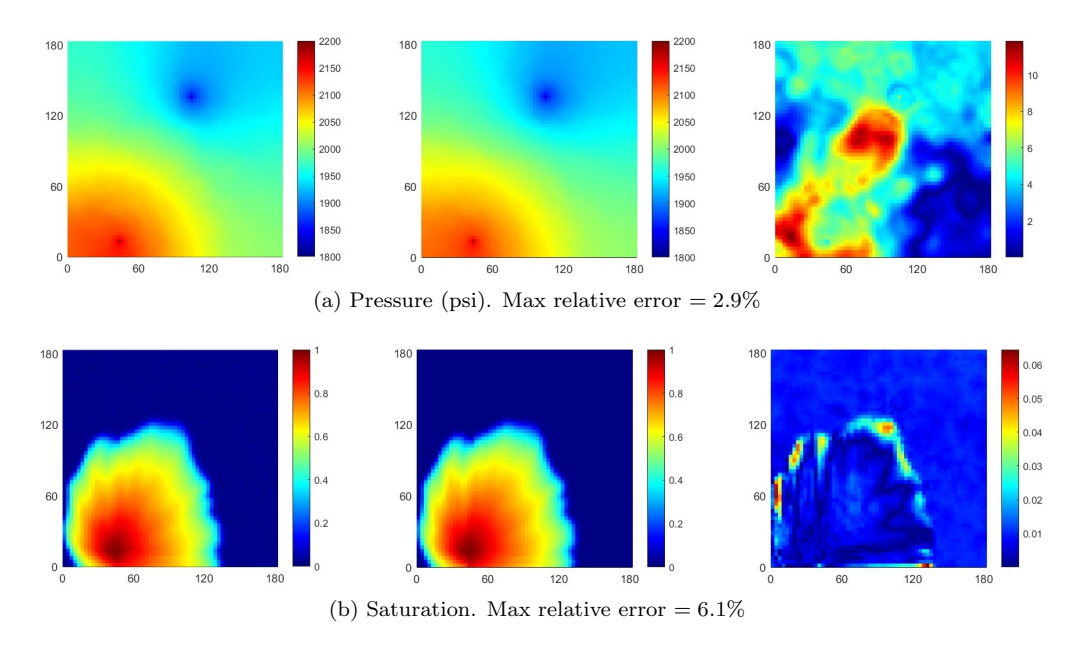


Figure 9: Prediction (left), ground truth (middle), and absolute difference (right) profiles of Case 3 on the regular Cartesian mesh.

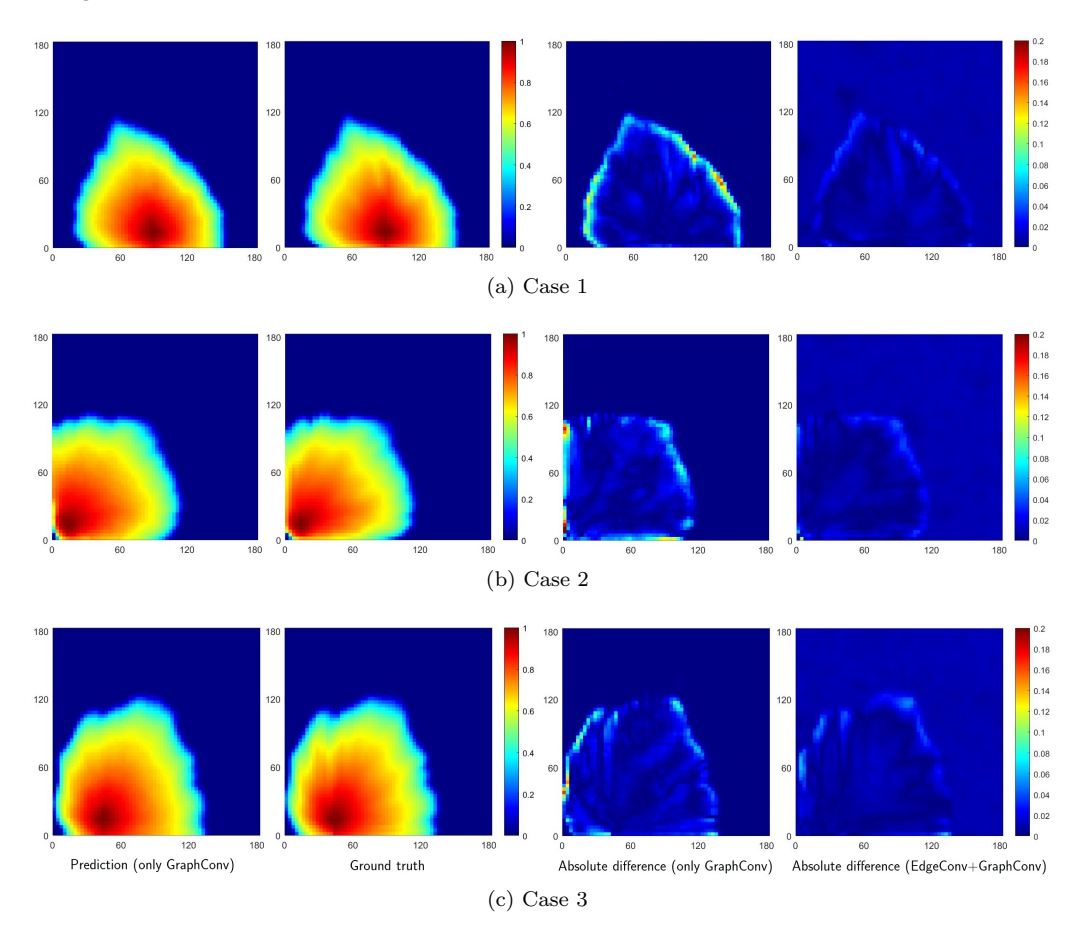


Figure 10: Prediction by the GCN model with only GraphConv, ground truth, and absolute difference profiles of the three cases on the regular Cartesian mesh.

Table 2: Mean relative saturation errors (averaged over the invaded region) of the three cases on the regular Cartesian mesh.

Saturation model	Case 1	Case 2	Case 3
(GraphConv)	1.89 %	1.68 %	1.32 %
(EdgeConv+GraphConv)	0.91 %	0.85 %	0.93 %

The solution profiles of the two cases are shown in Fig. 12 and Fig. 14, respectively. We can see that the surrogates predict the state evolutions with high accuracy. There is no significant saturation error from the predictions, except within certain regions near the domain boundaries. The results demonstrate that the Graph Convolutional Networks can generalize well to unseen domain geometries, even though our models were trained using only the data samples on a regular square domain.

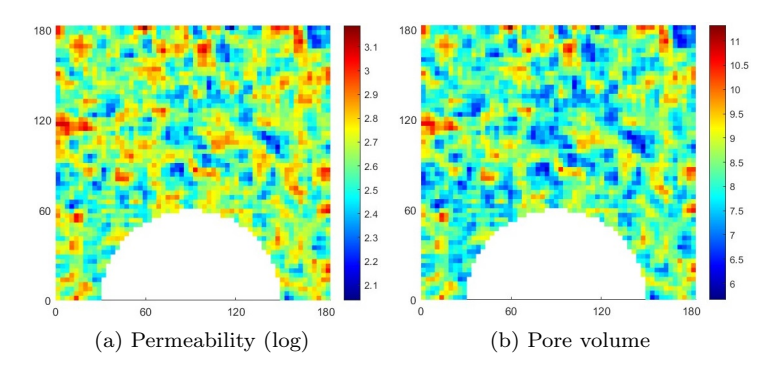


Figure 11: Permeability (md) and pore volume fields of Case 1 on irregular Cartesian mesh.

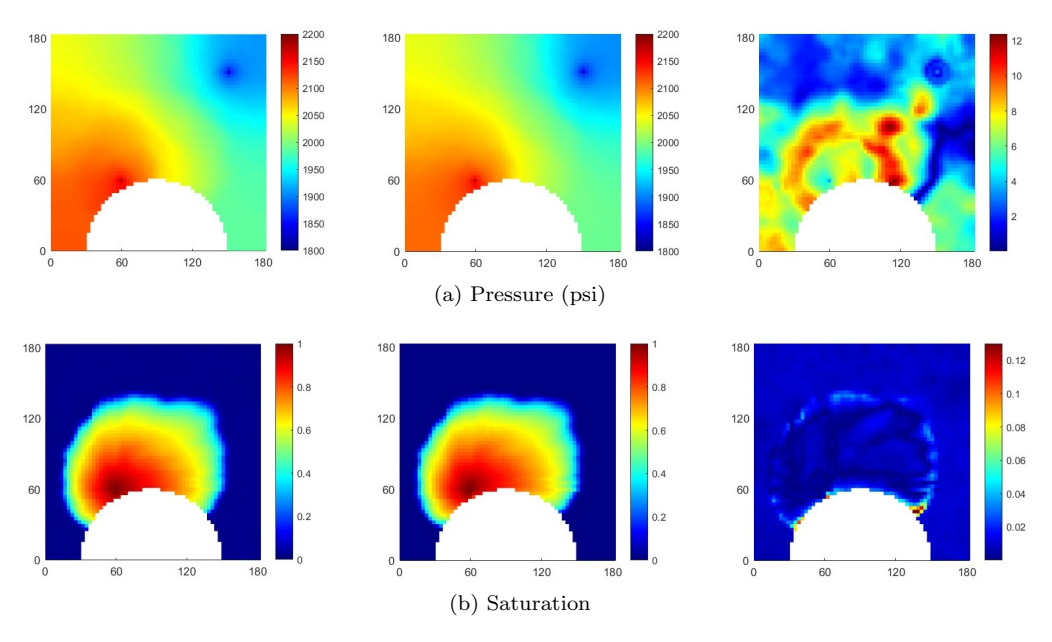


Figure 12: Prediction (left), ground truth (middle), and absolute difference (right) profiles of Case 1 on irregular Cartesian mesh.

7.3. PEBI mesh

Furthermore, we perform testing on a perpendicular bisector (PEBI) mesh with homogeneous permeability of 700 md and porosity of 0.3. Because the neighboring node

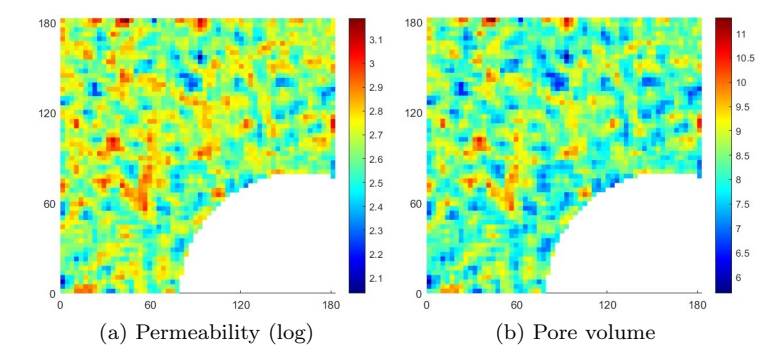


Figure 13: Permeability (md) and pore volume fields of Case 2 on irregular Cartesian mesh.

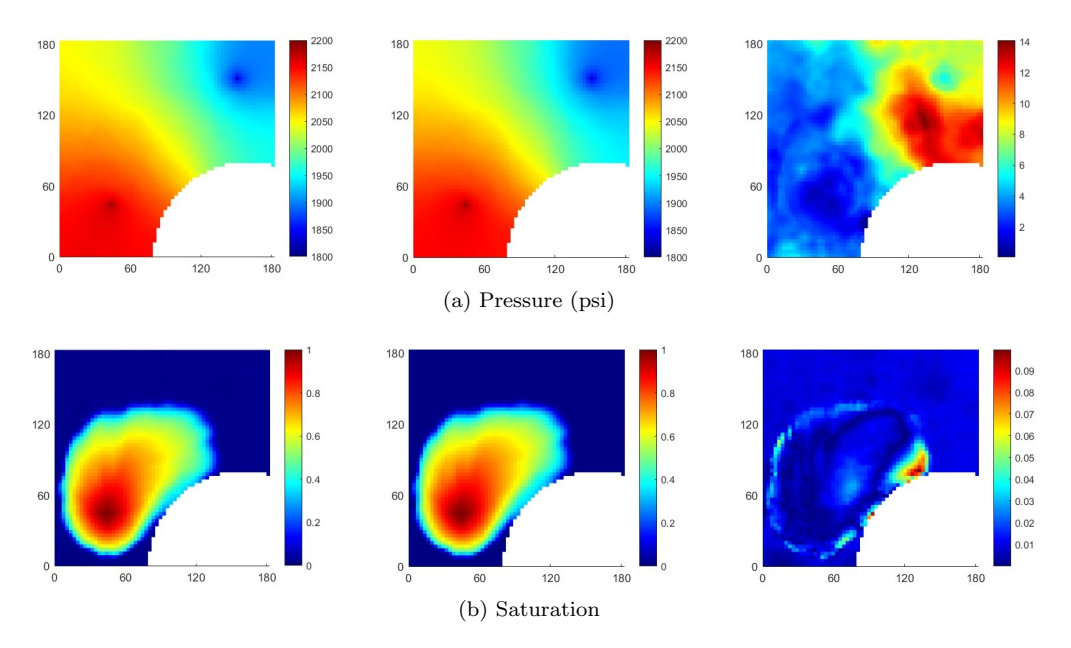


Figure 14: Prediction (left), ground truth (middle), and absolute difference (right) profiles of Case 2 on irregular Cartesian mesh.

numbers are different from the previous Cartesian meshes, we add 5 training samples with different rock properties and well locations on the PEBI mesh to improve prediction accuracy, adding up to a total of 165 samples in the new training dataset. A schematic of the PEBI mesh is plotted in **Fig. 15**. The solution profiles are shown in **Fig. 16**. Again, we can observe that the solutions from the surrogates closely match the high-fidelity simulation. Our GCN models generalize well to unstructured meshes, suggesting that the networks learn a general understanding of the physical processes of the multi-phase flow and transport PDE system.

8. Summary

We apply GCNs for surrogate modeling to approximate the spatial-temporal solutions of multi-phase flow and transport in porous media. We propose a new GCN architecture suited to the hyperbolic character of the coupled PDE system, to better capture the saturation dynamics. Our surrogate models can provide significant speedups (220 orders of magnitude) compared to the high-fidelity simulator.

The prediction performance of the trained surrogates and their generalization capabilities on out-of-training domain shapes and meshes are evaluated using 2D heterogeneous

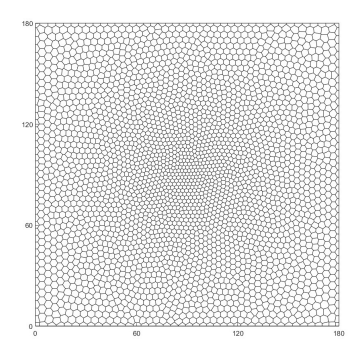


Figure 15: Schematic of the PEBI mesh.

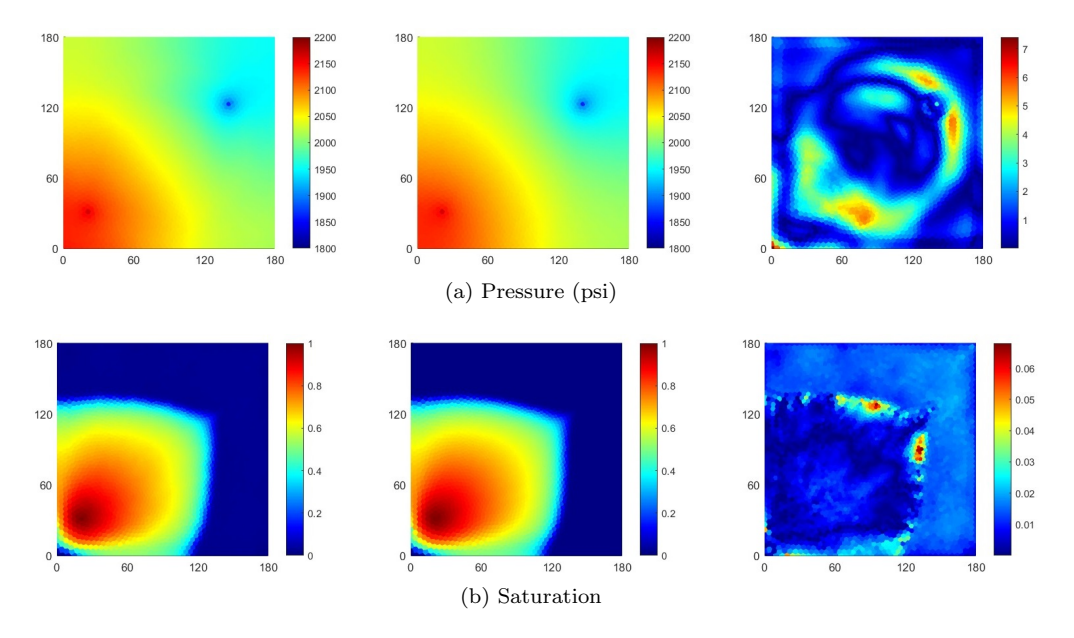


Figure 16: Prediction (left), ground truth (middle), and absolute difference (right) profiles of the case on the PEBI mesh.

test cases. The results show that our surrogates accurately predict the evolutions of the pressure and saturation states. Even though the models were trained on the next-step predictions, the rollouts remain stable for multiple timesteps. The saturation model based on the GCN architecture incorporating EdgeConv can reproduce both the shapes and heterogeneous details of the discontinuous saturation fronts with high accuracy. Moreover, we demonstrate that the GCN-based models generalize well to unseen domain geometries and unstructured meshes.

Acknowledgements

We thank Sidian Chen at The University of Arizona for constructive discussions.

References

Brenier, Y. and Jaffré, J., 1991. Upstream differencing for multiphase flow in reservoir simulation. SIAM journal on numerical analysis, 28(3), pp.685-696.

Battaglia, P., Pascanu, R., Lai, M. and Jimenez Rezende, D., 2016. Interaction networks for learning about objects, relations and physics. Advances in neural information processing systems, 29.

Bar-Sinai, Y., Hoyer, S., Hickey, J. and Brenner, M.P., 2019. Learning data-driven discretizations for partial differential equations. Proceedings of the National Academy of Sciences, 116(31), pp.15344-15349.

Belbute-Peres, F.D.A., Economon, T. and Kolter, Z., 2020, November. Combining differentiable PDE solvers and graph neural networks for fluid flow prediction. In international conference on machine learning (pp. 2402-2411). PMLR.

Brandstetter, J., Worrall, D. and Welling, M., 2022. Message passing neural PDE solvers. arXiv preprint arXiv:2202.03376.

Chen, J., Hachem, E. and Viquerat, J., 2021. Graph neural networks for laminar flow prediction around random two-dimensional shapes. Physics of Fluids, 33(12), p.123607.

Guo, X., Li, W. and Iorio, F., 2016, August. Convolutional neural networks for steady flow approximation. In Proceedings of the 22nd ACM SIGKDD international conference on knowledge discovery and data mining (pp. 481-490).

Gilmer, J., Schoenholz, S.S., Riley, P.F., Vinyals, O. and Dahl, G.E., 2017, July. Neural message passing for quantum chemistry. In International conference on machine learning (pp. 1263-1272). PMLR.

Iakovlev, V., Heinonen, M. and Lähdesmäki, H., 2020. Learning continuous-time pdes from sparse data with graph neural networks. arXiv preprint arXiv:2006.08956.

Jiang, Z., Tahmasebi, P. and Mao, Z., 2021. Deep residual U-net convolution neural networks with autoregressive strategy for fluid flow predictions in large-scale geosystems. Advances in Water Resources, 150, p.103878.

Kingma, D.P. and Ba, J., 2014. Adam: A method for stochastic optimization. arXiv preprint arXiv:1412.6980.

Kipf, T.N. and Welling, M., 2016. Semi-supervised classification with graph convolutional networks. arXiv preprint arXiv:1609.02907.

Krizhevsky, A., Sutskever, I. and Hinton, G.E., 2017. Imagenet classification with deep convolutional neural networks. Communications of the ACM, 60(6), pp.84-90.

Kutz, J.N., 2017. Deep learning in fluid dynamics. Journal of Fluid Mechanics, 814, pp.1-4.

LeCun, Y., Bengio, Y. and Hinton, G., 2015. Deep learning. nature, 521(7553), pp.436-444.

Long, Z., Lu, Y., Ma, X. and Dong, B., 2018, July. Pde-net: Learning pdes from data. In International conference on machine learning (pp. 3208-3216). PMLR.

Morris, C., Ritzert, M., Fey, M., Hamilton, W.L., Lenssen, J.E., Rattan, G. and Grohe, M., 2019, July. Weisfeiler and leman go neural: Higher-order graph neural networks. In Proceedings of the AAAI conference on artificial intelligence (Vol. 33, No. 01, pp. 4602-4609).

Mo, S., Zhu, Y., Zabaras, N., Shi, X. and Wu, J., 2019. Deep convolutional encoder-decoder networks for uncertainty quantification of dynamic multiphase flow in heterogeneous media. Water Resources Research, 55(1), pp.703-728.

Maldonado-Cruz, E. and Pyrcz, M.J., 2022. Fast evaluation of pressure and saturation predictions with a deep learning surrogate flow model. Journal of Petroleum Science and Engineering, 212, p.110244.

Maucec, M. and Jalali, R., 2022. GeoDIN-Geoscience-Based Deep Interaction Networks for Predicting Flow Dynamics in Reservoir Simulation Models. SPE Journal, 27(03), pp.1671-1689.

Peaceman, D.W., 1983. Interpretation of well-block pressures in numerical reservoir simulation with nonsquare grid blocks and anisotropic permeability. Society of Petroleum Engineers Journal, 23(03), pp.531-543.

Pfaff, T., Fortunato, M., Sanchez-Gonzalez, A. and Battaglia, P.W., 2020. Learning mesh-based simulation with graph networks. arXiv preprint arXiv:2010.03409.

Pilva, P. and Zareei, A., 2022. Learning time-dependent PDE solver using Message Passing Graph Neural Networks. arXiv preprint arXiv:2204.07651.

Sammon, P.H., 1988. An analysis of upstream differencing. SPE reservoir engineering, 3(03), pp.1-053.

Sanchez-Gonzalez, A., Godwin, J., Pfaff, T., Ying, R., Leskovec, J. and Battaglia, P., 2020, November. Learning to simulate complex physics with graph networks. In International conference on machine learning (pp. 8459-8468). PMLR.

Santos, J.E., Xu, D., Jo, H., Landry, C.J., Prodanović, M. and Pyrcz, M.J., 2020. PoreFlow-Net: A 3D convolutional neural network to predict fluid flow through porous media. Advances in Water Resources, 138, p.103539.

Tang, M., Liu, Y. and Durlofsky, L.J., 2020. A deep-learning-based surrogate model for data assimilation in dynamic subsurface flow problems. Journal of Computational Physics, 413, p.109456.

Vinuesa, R. and Brunton, S.L., 2022. Enhancing computational fluid dynamics with machine learning. Nature Computational Science, 2(6), pp.358-366.

Wang, Y., Sun, Y., Liu, Z., Sarma, S.E., Bronstein, M.M. and Solomon, J.M., 2019. Dynamic graph cnn for learning on point clouds. Acm Transactions On Graphics (tog), 38(5), pp.1-12.

Wang, Y. and Lin, G., 2020. Efficient deep learning techniques for multiphase flow simulation in heterogeneous porousc media. Journal of Computational Physics, 401, p.108968.

Wen, G., Hay, C. and Benson, S.M., 2021. CCSNet: a deep learning modeling suite for CO2 storage. Advances in Water Resources, 155, p.104009.

Yan, B., Harp, D.R., Chen, B., Hoteit, H. and Pawar, R.J., 2022. A gradient-based deep neural network model for simulating multiphase flow in porous media. Journal of Computational Physics, 463, p.111277.

Zhang, K., Wang, Y., Li, G., Ma, X., Cui, S., Luo, Q., Wang, J., Yang, Y. and Yao, J., 2021. Prediction of field saturations using a fully convolutional network surrogate. SPE Journal, 26(04), pp.1824-1836.